IOP Publishing Physical Biology
Phys. Biol. 11 (2014) 026001 (15pp) doi:10.1088/1478-3975/11/2/026001

Deciphering the axonal transport kinetics of neurofilaments using the fluorescence photoactivation pulse-escape method

Yinyun Li[1], **Anthony Brown**[2] **and Peter Jung**[1]

[1] Quantitative Biology Institute, Ohio University, Athens, OH 45701, USA
[2] Department of Neuroscience, The Ohio State University, Columbus, OH 43210, USA

E-mail: jungp@ohio.edu and brown.2302@osu.edu

Received 23 October 2013, revised 9 January 2014
Accepted for publication 11 February 2014
Published 17 March 2014

Abstract

Neurofilaments are transported along axons stochastically in a stop-and-go manner, cycling between brief bouts of rapid movement and pauses that can vary from seconds to hours in length. Presently the only way to analyze neurofilament pausing experimentally on both long and short time scales is the pulse-escape method. In this method, fluorescence photoactivation is used to mark a population of axonal neurofilaments and then the loss of fluorescence from the activated region due to neurofilament movement is monitored by time-lapse imaging. Here we develop a mathematical description of the pulse-escape kinetics in terms of the rate constants of a tested mathematical model and we show how this model can be used to characterize neurofilament transport kinetics from fluorescence photoactivation pulse-escape experiments. This combined experimental and computational approach is a powerful tool for the analysis of the moving and pausing behavior of neurofilaments in axons.

Keywords: axon, neurofilament, cytoskeleton, slow axonal transport, mathematical modeling

1. Introduction

Neurofilaments, which are the intermediate filaments of nerve cells, are abundant space-filling cytoskeletal polymers that function to increase axonal caliber, thereby increasing the rate of propagation of the nerve impulse. These polymers are assembled in the neuronal cell body and are transported along axons in the slowest phase of axonal transport, known as slow axonal transport, at average velocities of 0.2–3 mm d^{-1} [1]. For many years, it was assumed that this is a slow and continuous movement [2], but it is now believed to be caused by brief bouts of rapid movement interrupted by pauses that can vary from seconds to hours in length [3–5]. The filaments move both forward (anterograde) and backwards (retrograde) along microtubule tracks, but the net direction is anterograde because anterograde movements predominate. The slow average velocity is caused by these bidirectional excursions as well as the large fraction of time that the neurofilaments spend pausing.

The kinetics of neurofilament transport can be studied in nerves on a time scale of days or months using radioisotopic pulse-labeling, or in single axons on a time scale of seconds, minutes or hours using fluorescence microscopy [1, 6]. One fluorescence microscopic technique involves real-time or time-lapse imaging of single-neurofilament polymers tagged with fluorescent fusion proteins [7]. Since neurofilaments are just 10 nm in diameter and are typically spaced just tens of nanometers apart from each other in axons, the only way to track their movement by fluorescence microscopy is to observe them in isolation. Practically, this can be accomplished in cultured neurons by observing neurofilament movement through naturally occurring or photobleached gaps in the axonal neurofilament array [7–10]. When fluorescently tagged neurofilaments enter these gaps they can be resolved because they are the only fluorescent structures. However, it is important to note that this method tends to underestimate the long-term pausing behavior of the filaments because only those filaments that move into the gaps can be tracked.

To address the limitations of single-neurofilament tracking experiments, we developed a complementary fluorescence microscopic technique that permits a population-level analysis of neurofilament transport kinetics in single

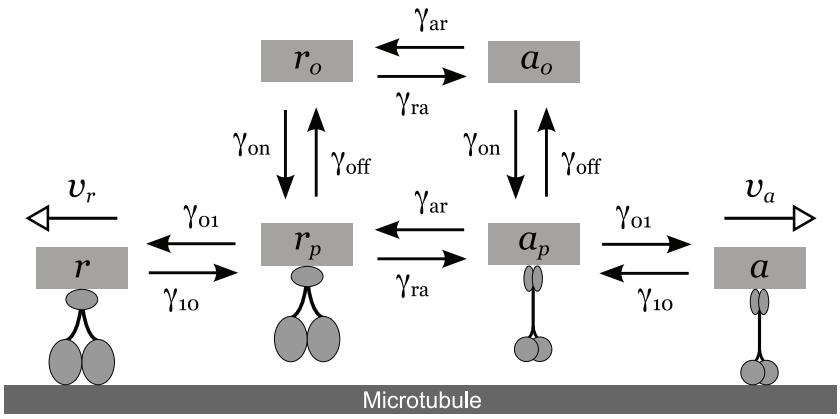

Figure 1. A six-state kinetic model of neurofilament transport. Cartoon depicting one interpretation of the various kinetic states. There are four on-track states (a, a_0, r, r_0) and two off-track states (a_p, r_p). On-track neurofilaments move along microtubules in an anterograde or retrograde direction (states a and r, respectively) with velocities v_a and v_r. The anterograde movements are powered by kinesin motors and the retrograde movements by dynein motors. While in the on-track moving states, the filaments can switch to on-track pausing states a_0 and r_0, governed by the rate γ_{10}. When in the on-track pausing states, the filaments can either switch back to their respective on-track moving states, governed by the rate γ_{01}, or they can switch to the corresponding off-track pausing states a_p or r_p. Cycling between the on and off-track pausing states is governed by the rates γ_{off} and γ_{on}. Reversals can happen in all pausing states, governed by the reversal rate constants, γ_{ar} and γ_{ra}.

axons [11]. This fluorescence photoactivation pulse-escape method uses photoactivation of neurofilament polymers tagged with a photoactivatable fluorescent fusion protein to create a population of fluorescent neurofilaments in a short segment of axon. Over time the fluorescence in the activated region declines due to the rapid intermittent movement of the photoactivated neurofilament polymers, and this can be tracked by time-lapse imaging. Since there is little soluble neurofilament protein in axons, there is no measurable contribution of diffusion to the loss of fluorescence and therefore the decay kinetics are due entirely to neurofilament transport [11]. In the current paper, we develop an analytical solution of the pulse-escape decay kinetics in terms of the rate constants of a tested mathematical model and we present a computational method for extracting the kinetic parameters of neurofilament transport in fluorescence photoactivation pulse-escape experiments on short and long time scales.

2. A mathematical model of neurofilament transport

The first mathematical model of neurofilament transport was proposed by Blum and Reed [12]. That model, which predated the observation of neurofilament movement by live-cell imaging, assumed the existence of a hypothetical engine that moved unidirectionally at a fixed velocity. Microtubules were considered to interact directly with the engine and neurofilaments were considered to move by riding piggy-back on the moving microtubules. By computational simulation of the equations of the model, the authors were able to reproduce the bell-shaped waves of radiolabeled neurofilaments observed in radioactive pulse-labeling experiments *in vivo*. More recently, we have described a mathematical model for neurofilament kinetics that reproduces the motile behavior of single neurofilaments observed by time-lapse imaging of cultured neurons on a time scale of second or minutes as well as the bell-shaped waves observed for large ensembles by radioisotopic pulse-labeling on a time scale of days or weeks [13, 14]. This model invokes six kinetic states (see figure 1): anterograde and retrograde moving states (a, r), anterograde and retrograde short-term pausing states (a_0, r_0), and anterograde and retrograde long-term pausing states (a_p, r_p). In the anterograde and retrograde moving states, the neurofilaments are driven by molecular motors (kinesins and dyneins) along microtubule tracks. The short-term pausing states were introduced to generate the observed bursts of rapid intermittent movement observed in single-neurofilament tracking experiments in cultured neurons on a time course of seconds or minutes. The long-term pausing states, not visible in the short-term single filament tracking experiments, were introduced to reproduce waves of radiolabeled neurofilaments observed in radioisotopic pulse-labeling experiments *in vivo* on a time course of weeks or months [13] and were verified later in cultured neurons using the fluorescence photoactivation pulse-escape technique [11]. We refer to the short-term and long-term pausing states as 'on-track' and 'off-track' respectively [11] (see section 7). Note, however, that a model in which there is just a single long-term pausing state can also reproduce the bell-shaped waves in radioisotopic pulse-labeling experiments [15].

We should point out that the mathematics of the types of partial differential equations that are used in the model in [14] and in this study are well-developed and mathematical models used for fast axonal transport of organelles (e.g. [16]) have similar structure. For example, traveling wave solutions of these partial differential equations have been discussed in [17] and [18], and proofs of the existence of solutions to these equations can be found in [19]. Times of equilibration have been discussed for a two-state model [20]. The time of transit of motor driven particles transported from a source to a target along an axon has been addressed using a three-state model (anterograde movement, retrograde movement, pausing) in [21, 22] and a two-state model for NMDA receptor trafficking in axons has been discussed in [23].

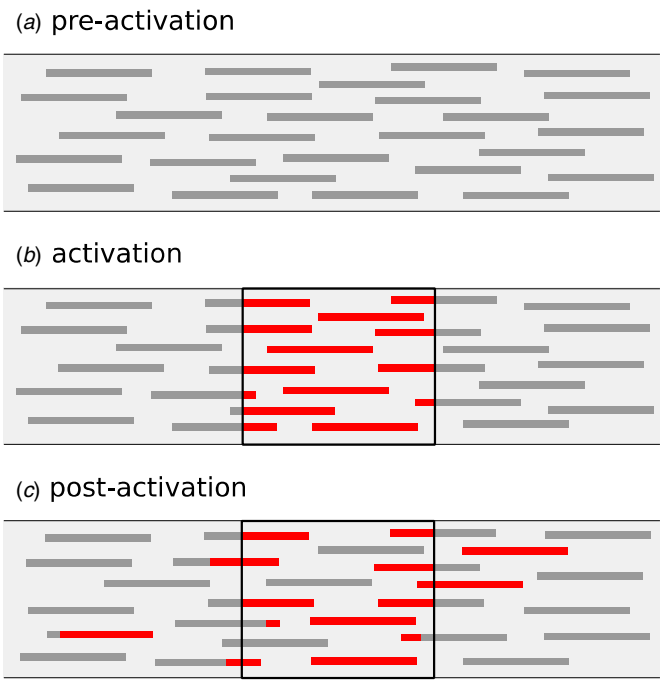

Figure 2. Schematic diagram of a pulse-escape experiment. (*a*) Before activation the axon contains non-activated (i.e. non-fluorescent) neurofilaments tagged with photoactivatable GFP (dark gray lines). (*b*) Photoactivation causes the neurofilaments within the activated region (black rectangle) to become fluorescent (red lines). (*c*) After photoactivation, the rapid intermittent movement of the neurofilaments causes fluorescent neurofilaments to move out of the activated region and non-fluorescent neurofilaments to move in. The kinetics of the loss of fluorescence in the activated region reflects the kinetics of departure of the activated neurofilaments. Note that while in principle neurofilaments that have left the window can return, in practice this happens rarely because the frequency of reversals is low.

3. The pulse-escape method

In contrast to the analysis of neurofilament movement through photobleached or naturally occurring gaps in the axonal neurofilament array, the pulse-escape method is a population-based approach [11] (figure 2). While it is possible to track the escape of individual filaments from the activated regions on time scales of seconds or minutes [11], the real power of this technique comes from tracking the loss of the fluorescence on a time scale of several hours. When we do this we consistently observe a biphasic decay profile [11, 24]. Initially there is a more rapid decrease in the fluorescence within the activation window due to the departure of neurofilaments that are moving on-track at the time of activation. At later times, there is a slower decline in the fluorescence due to the departure of neurofilaments that are immobile (off-track) at the time of activation and which can only escape the window after they have cycled into the mobile state. Hence, the time course of fluorescence decay at longer times reflects the fraction of neurofilaments that are pausing off-track at the time of activation and their rate of transition into the mobile states. Thus we conjecture that the overall time course of fluorescence decay from the activation window holds complete information about the neurofilament transport kinetics and that tracking the fluorescence decay on a time scale of several hours should therefore reveal the pausing behavior of neurofilaments residing within the activation window on that time scale.

In the following sections we develop a systematic computational method to extract the rate constants in our mathematical model of neurofilament transport from the fluorescence photoactivation pulse-escape experiments and we show how this can be used to characterize the moving and pausing behavior of neurofilaments in axons. To explore the utility of this approach, we analyze two published pulse-escape data sets for neurofilaments, one from axons of cultured neurons from the superior cervical ganglia (SCG) of newborn rats [11] and the other from the dorsal root ganglia (DRG) of newborn mice [24]. Each of these neuronal cell types exhibits biphasic pulse-escape decay kinetics that can be fit with a double-exponential function, but with different small and large exponents (figure 3).

4. Mathematical modeling of the pulse-escape experiment

In order to interpret the decay curves in figure 3, we mimic a pulse-escape experiment using a continuous representation of our six-state model for the neurofilament transport kinetics. The equations of motion are given by

$$\frac{\partial \rho_a}{\partial t} = -v_a \frac{\partial \rho_a}{\partial x} - \gamma_{10}\rho_a + \gamma_{01}\rho_{a0} \tag{1}$$

$$\frac{\partial \rho_r}{\partial t} = -v_r \frac{\partial \rho_r}{\partial x} - \gamma_{10}\rho_r + \gamma_{01}\rho_{r0} \tag{2}$$

$$\frac{\partial \rho_{a0}}{\partial t} = -(\gamma_{01} + \gamma_{\mathrm{ar}} + \gamma_{\mathrm{off}})\rho_{a0} + \gamma_{10}\rho_a + \gamma_{\mathrm{ra}}\rho_{r0} + \gamma_{\mathrm{on}}\rho_{\mathrm{ap}} \tag{3}$$

$$\frac{\partial \rho_{r0}}{\partial t} = -(\gamma_{01} + \gamma_{\mathrm{ra}} + \gamma_{\mathrm{off}})\rho_{r0} + \gamma_{10}\rho_r + \gamma_{\mathrm{ar}}\rho_{a0} + \gamma_{\mathrm{on}}\rho_{\mathrm{rp}} \tag{4}$$

$$\frac{\partial \rho_{\mathrm{ap}}}{\partial t} = -(\gamma_{\mathrm{on}} + \gamma_{\mathrm{ar}})\rho_{\mathrm{ap}} + \gamma_{\mathrm{off}}\rho_{a0} + \gamma_{\mathrm{ra}}\rho_{\mathrm{rp}} \tag{5}$$

$$\frac{\partial \rho_{\mathrm{rp}}}{\partial t} = -(\gamma_{\mathrm{on}} + \gamma_{\mathrm{ra}})\rho_{\mathrm{rp}} + \gamma_{\mathrm{off}}\rho_{r0} + \gamma_{\mathrm{ar}}\rho_{\mathrm{ap}}, \tag{6}$$

where v_a and v_b denote the anterograde and retrograde velocities of the moving filaments, and ρ_a, ρ_{a0}, ρ_{ap}, ρ_r, ρ_{r0}, ρ_{rp} denote the distributions of the neurofilaments in the kinetic states a, a_0, a_{p}, r, r_0, r_{p} along the axon length x. The rate constants γ_{01}, γ_{10}, γ_{off}, γ_{on}, γ_{ar} and γ_{ra} are defined in figure 1. If neurofilaments enter the axon at the proximal end at a rate j_{in}, the uniform equilibrium distributions of neurofilaments in the kinetic states can be obtained readily by solving equations (1)–(6), i.e.

$$\rho_a = (j_{\mathrm{in}}/v_a);\ \rho_{a0} = q_1(j_{\mathrm{in}}/v_a);\ \rho_{\mathrm{ap}} = q_1 q_2 (j_{\mathrm{in}}/v_a)$$
$$\rho_r = q_3(j_{\mathrm{in}}/v_a);\ \rho_{r0} = q_1 q_3 (j_{\mathrm{in}}/v_a);\ \rho_{\mathrm{rp}} = q_1 q_2 q_3 (j_{\mathrm{in}}/v_a), \tag{7}$$

with

$$q_1 \equiv \gamma_{10}/\gamma_{01};\ q_2 \equiv \gamma_{\mathrm{off}}/\gamma_{\mathrm{on}};\ q_3 \equiv \gamma_{\mathrm{ar}}/\gamma_{\mathrm{ra}}. \tag{8}$$

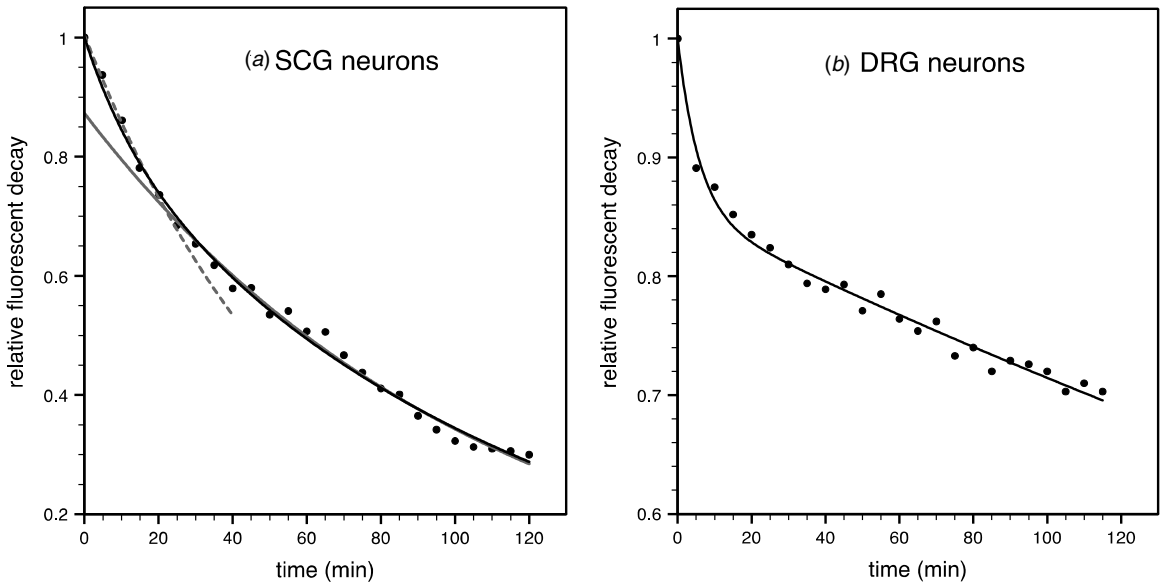

Figure 3. Pulse-escape kinetics for (*a*) cultured rat superior cervical ganglion (SCG) neurons and (*b*) cultured mouse dorsal root ganglion (DRG) neurons. Data from [11] and [24]. The solid black lines represent curve fits using a double exponential function of the form $A_1 \exp(-t/\tau_1) + A_2 \exp(-t/\tau_2)$. The fitting parameters are $A_1 = 0.849$, $A_2 = 0.160$, $\tau_1 = 111$ min and $\tau_2 = 11.8$ min for the SCG neurons and $A_1 = 0.854$, $A_2 = 0.142$, $\tau_1 = 562$ min and $\tau_2 = 5.89$ min for the DRG neurons. The average activation window length was 22 μm for the SCG neurons and 24.5 μm for the DRG neurons. To better indicate the double exponential behavior of the data in (*a*) we show the exponential fits for small times (dashed, gray) and large times (full, gray).

In terms of the total neurofilament distribution (summated over all states)

$$\begin{aligned}\rho &\equiv \rho_a + \rho_{a0} + \rho_{\mathrm{ap}} + \rho_r + \rho_{r0} + \rho_{\mathrm{rp}} \\ &= (j_{\mathrm{in}}/v_a)(1 + q_1(1 + q_2))(1 + q_3),\end{aligned} \tag{9}$$

we can write

$$\begin{aligned}&\rho_a = \eta\rho;\ \rho_{a0} = \eta q_1\rho;\ \rho_{\mathrm{ap}} = \eta q_1 q_2 \rho \\ &\rho_r = \eta q_3\rho;\ \rho_{r0} = \eta q_1 q_3 \rho;\ \rho_{\mathrm{rp}} = \eta q_1 q_2 q_3 \rho,\end{aligned} \tag{10}$$

with

$$\eta \equiv \frac{1}{(1 + q_1(1 + q_2))(1 + q_3)}. \tag{11}$$

Before the neurofilaments (tagged with photoactivatable green fluorescent protein) are photo-activated, we assume that their kinetic states obey the equilibrium distributions in (7). At the activation time $t = 0$, all neurofilaments within an activation window extending between position $x = 0$ and $x = a$ along the axon are activated. As in the experimental protocol, we follow the distribution of the photoactivated neurofilaments only (the other ones are invisible) using equations (1)–(6), utilizing the linear superposition principle valid for sets of linear equations. The fluorescence within the activation window, which is a relative measure of the neurofilament content, is then given by

$$\begin{aligned}Q(t) = \int_0^a &(\rho_a(x,t) + \rho_{a0}(x,t) + \rho_{\mathrm{ap}}(x,t) \\ &+ \rho_r(x,t) + \rho_{r0}(x,t) + \rho_{\mathrm{rp}}(x,t))\,\mathrm{d}x.\end{aligned} \tag{12}$$

Before we engage with a mathematical analysis of $Q(t)$, we will discuss numerical solutions of equations (1)–(6) and their subsequent integration according to equation (12). The results are shown in figure 4 for an arbitrary, though not atypical, set of rate constants. As in the experiments, we observe an initial rapid decay due to the departure of neurofilaments in the mobile (on-track) state followed by a slower exponential decay due to the mobilization of filaments that were initially in the immobile (off-track) state. In principle, the decay kinetics could be affected by reversals because this could allow neurofilaments that have left the activated region to re-enter. However, we have shown previously that neurofilament reversals are rare [8, 9, 25], with rough estimates for γ_{ra} and γ_{ar} of $<1 \times 10^{-4}$ s^{-1} based on live imaging studies and computational modeling [13, 14]. To examine the influence of reversals on the decay kinetics, we simulated pulse-escape experiments over a 33 h period using values for γ_{ra} and γ_{ar} ranging from 10^{-5} to 10^{-7} s^{-1} (see inset in figure 4). The curves deviate from the normal long-term exponential decay at later times, with the time of the divergence being earlier for higher reversal rates. However, the curves are indistinguishable in the first several hours after activation, which is the typical duration of our pulse-escape experiments, and thus we can ignore reversal events in the following analysis.

Continuing with our mathematical analysis we take the derivative of equation (12) with respect to time, utilizing equations (1)–(6), and find the following relation:

$$\frac{\mathrm{d}Q}{\mathrm{d}t} = -v_a(\rho_a(a,t) - \rho_a(0,t)) - v_r(\rho_r(a,t) - \rho_r(0,t)). \tag{13}$$

Because of the convective nature of equations (1) and (2), and because initially $\rho_a(x < 0, 0) = 0$ and $\rho_r(x > a, 0) = 0$ (i.e. neurofilaments outside the activation window are not activated) it is clear that $\rho_a(0,t) = 0$ and $\rho_r(a,t) = 0$, yielding

$$\frac{\mathrm{d}Q}{\mathrm{d}t} = -v_a\rho_a(a,t) + v_r\rho_r(0,t). \tag{14}$$

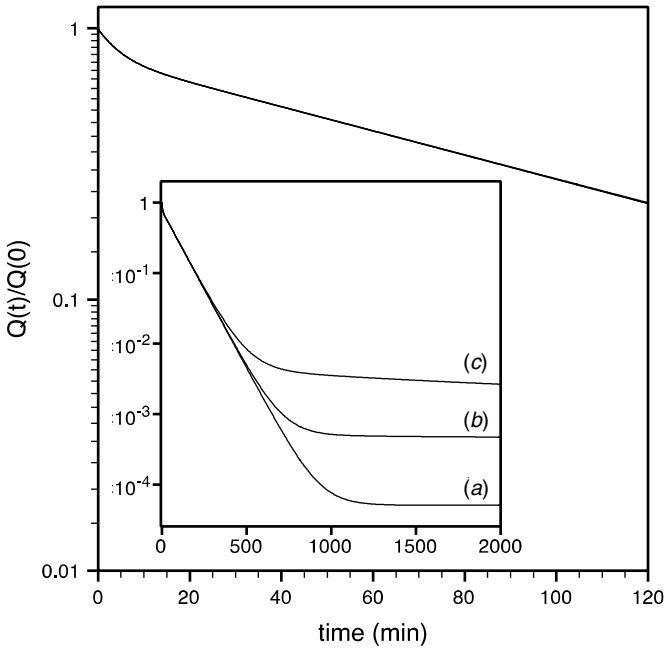

Figure 4. Dependence of the decay kinetics on the reversal rates. Simulations of the relative fluorescence decay $Q(t)/Q(0)$ within an activation window of length $a = 10$ μm using the rate constants $\gamma_{10} = 0.05$ s^{-1}, $\gamma_{01} = 0.005$ s^{-1}, $\gamma_{\rm off} = 5.0 \times 10^{-4}$ s^{-1} and $\gamma_{\rm on} = 2.0 \times 10^{-4}$ s^{-1} for three different sets of reversal rate constants, i.e. (*a*) $\gamma_{\rm ar} = 1.0 \times 10^{-7}$ s^{-1} and $\gamma_{\rm ra} = 2.0 \times 10^{-7}$ s^{-1}, (*b*) $\gamma_{\rm ar} = 1.0 \times 10^{-6}$ s^{-1} and $\gamma_{\rm ra} = 2.0 \times 10^{-6}$ s^{-1} and (*c*) $\gamma_{\rm ar} = 1.0 \times 10^{-5}$ s^{-1} and $\gamma_{\rm ra} = 2.0 \times 10^{-5}$ s^{-1}, with the ratio $\gamma_{\rm ar}/\gamma_{\rm ra} = 0.5$ in each case. The decay curves are superimposable at early times (<300 min), with a faster initial decay followed by a slower exponential decay. At longer times (>300 min), the curves transition to an even slower exponential decay due to the influence of the reversals and diverge in a manner dependent on the reversal frequency.

Ignoring reversals (see above), we can split the set of equations (1)–(6) into two sets of linear equations, one anterograde and one retrograde:

$$\frac{\partial \rho_a}{\partial t} = -v_a \frac{\partial \rho_a}{\partial x} - \gamma_{10}\rho_a + \gamma_{01}\rho_{a0} \tag{15}$$

$$\frac{\partial \rho_{a0}}{\partial t} = -(\gamma_{01} + \gamma_{\rm off})\rho_{a0} + \gamma_{10}\rho_a + \gamma_{\rm on}\rho_{\rm ap} \tag{16}$$

$$\frac{\partial \rho_{\rm ap}}{\partial t} = -\gamma_{\rm on}\rho_{\rm ap} + \gamma_{\rm off}\rho_{a0}, \tag{17}$$

and

$$\frac{\partial \rho_r}{\partial t} = -v_r \frac{\partial \rho_r}{\partial x} - \gamma_{10}\rho_r + \gamma_{01}\rho_{r0} \tag{18}$$

$$\frac{\partial \rho_{r0}}{\partial t} = -(\gamma_{01} + \gamma_{\rm off})\rho_{r0} + \gamma_{10}\rho_r + \gamma_{\rm on}\rho_{\rm rp} \tag{19}$$

$$\frac{\partial \rho_{\rm rp}}{\partial t} = -\gamma_{\rm on}\rho_{\rm rp} + \gamma_{\rm off}\rho_{r0}, \tag{20}$$

which can be solved separately.

To obtain insights into how to interpret the experimental decay curves in terms of the rate constants of the model, we consider $Q(t)$ separately for small times and for large times. Since the governing equations (1)–(6) are linear we can perform a Laplace transformation [26] of equations (15)–(20) with respect to time, i.e.

$$\tilde{\rho}_{a,r,a0,r0,{\rm ap},{\rm rp}}(x,s) = \int_0^\infty \rho_{a,r,a0,r0,{\rm ap},{\rm rp}}(x,t)\exp(-st)\,{\rm d}t, \tag{21}$$

and eliminate all functions, except $\tilde{\rho}_a(s,x)$ and $\tilde{\rho}_r(s,x)$ to find

$$\tilde{\rho}_a(x,s) = \frac{\rho\eta}{s}\left(1 - \exp\left(-\frac{sf(s)}{v_a}x\right)\right)$$
$$\tilde{\rho}_r(x,s) = \frac{q_3\rho\eta}{s}\left(1 - \exp\left(-\frac{sf(s)}{v_r}(x-a)\right)\right). \tag{22}$$

Note that the reversal rate ratio q_3 enters into (22) even though we neglect reversals because it determines the relative proportion of neurofilaments in the anterogradely and retrogradely moving states (equation (10)). A Laplace transformation of the fluorescence in the activated region $Q(t)$ (see equation (12)) yields

$$\tilde{Q}(s) = \frac{a\rho}{s} - \frac{v_a\eta\rho}{s^2}\left(1 - \exp\left(-\frac{sf(s)}{v_a}a\right)\right)$$
$$+\frac{v_r q_3\eta\rho}{s^2}\left(1 - \exp\left(\frac{sf(s)}{v_r}a\right)\right), \tag{23}$$

with η defined in equation (11), and

$$f(s) = 1 + \gamma_{10}\frac{s + \gamma_{\rm on} + \gamma_{\rm off}}{s^2 + s(\gamma_{01} + \gamma_{\rm on} + \gamma_{\rm off}) + \gamma_{01}\gamma_{\rm on}}. \tag{24}$$

4.1. The decay at short times

First we consider the pulse-escape decay kinetics at short times after activation. We expand $f(s)$ and $\tilde{Q}(s)$ into a Taylor series in powers of $1/s$ and then perform an inverse Laplace transformation (see appendix A for details). After some lengthy calculations, we find

$$\frac{Q(t)}{Q(0)} = 1 - \eta\left(\Theta\left(t - \frac{a}{v_a}\right)\exp(-\varepsilon_a)\right.$$
$$\left.+q_3\Theta\left(t + \frac{a}{v_r}\right)\exp(\varepsilon_r)\right) - \frac{\eta}{a}(v_a - q_3 v_r)\,t$$
$$+\frac{\eta}{a}\left(v_a\exp(-\varepsilon_a)\Theta\left(t - \frac{a}{v_a}\right) - v_r q_3\exp(\varepsilon_r)\Theta\left(t + \frac{a}{v_r}\right)\right)t$$
$$+\frac{1}{2}\eta\gamma_{10}\gamma_{01}\exp(-\varepsilon_a)\left(t - \frac{a}{v_a}\right)^2\Theta\left(t - \frac{a}{v_a}\right)$$
$$+\frac{1}{2}\eta q_3\gamma_{10}\gamma_{01}\exp(\varepsilon_r)\left(t + \frac{a}{v_r}\right)^2\Theta\left(t + \frac{a}{v_r}\right) \tag{25}$$

with

$$\varepsilon_a = \frac{a\gamma_{10}}{v_a}, \quad \varepsilon_r = \frac{a\gamma_{10}}{v_r}, \tag{26}$$

and the Heaviside step function $\Theta(x)$ given by

$$\Theta(x) = \begin{cases} 1 & \text{for} \quad x > 0 \\ 0 & \text{for} \quad x < 0 \end{cases}.$$

The average velocity of neurofilament movement was derived in [14] and is given by

$$\bar{v} = \frac{\gamma_{\mathrm{ra}} v_a + \gamma_{\mathrm{ar}} v_r}{(1 + q_1(1 + q_2))(\gamma_{\mathrm{ar}} + \gamma_{\mathrm{ra}})}. \tag{27}$$

The slope α of $Q(t)/Q(0)$ for $t < a/v_a$ and $t < a/|v_r|$ (see second term on the right-hand side of equation (25)), is linearly related to the average velocity (27) by

$$\alpha = \frac{1}{a}\frac{1 - q_3(v_r/v_a)}{1 + q_3(v_r/v_a)}\bar{v}. \tag{28}$$

Note that this indicates that the slope of the decay curve at short times is dependent on the length a of the activation window in addition to the velocities. In the special case where $v_a = -v_r \equiv v$ and $\varepsilon_a \equiv -\varepsilon_r \equiv \varepsilon$, equation (25) reduces to

$$\frac{Q(t)}{Q(0)} = \begin{cases} 1 - \frac{v}{a}\frac{1}{1+q_1(1+q_2)}t = 1 - \alpha t & \text{for} \quad t < a/v \\ 1 - \frac{\exp(-\varepsilon)}{1+q_1(1+q_2)} - \frac{v}{a}\frac{1-\exp(-\varepsilon)}{1+q_1(1+q_2)}t & \\ \quad + \frac{1}{2}\gamma_{10}\gamma_{01}\frac{\exp(-\varepsilon)}{1+q_1(1+q_2)}\left(t - \frac{a}{v}\right)^2 & \text{for} \quad t > a/v \end{cases}, \tag{29}$$

with the average velocity in this case

$$\bar{v} = \frac{v}{1 + q_1(1 + q_2)}\left(\frac{\gamma_{\mathrm{ra}} - \gamma_{\mathrm{ar}}}{\gamma_{\mathrm{ra}} + \gamma_{\mathrm{ar}}}\right) = \alpha a\left(\frac{1 - q_3}{1 + q_3}\right), \tag{30}$$

and $\varepsilon \equiv a\gamma_{10}/v$.

For times $t < a/v$ (i.e. less than the time it takes a moving neurofilament to escape the activation window), the decay is linear with a slope α (i.e. proportional to the average neurofilament velocity). For small activation windows (e.g. a few micrometers in length), this corresponds to a time interval a/v on the order of seconds. At time $t = a/v$, the slope changes discontinuously by the factor $1-\exp(-\varepsilon)$. For small activation windows or smaller values of γ_{10} (i.e. if ε is small), this change in slope is noticeable (see arrow in inset in figure 5).

4.2. The decay at long times

Now we consider the pulse-escape decay kinetics at longer times. The linearity of the curves on a log-scale at long times indicates an exponential decay (see figure 4) and thus we can extract the asymptotic exponential decay for $t \to \infty$, i.e.

$$Q(t) = Q_\infty \exp(-\gamma_d t) \tag{31}$$

with a decay constant γ_d obtained directly from the Laplace transform $\tilde{Q}(s)$ by expanding it for small s, i.e.

$$\tilde{Q}(s) = Q_\infty \frac{1}{s + \gamma_d} \approx \frac{Q_\infty}{\gamma_d}\left(1 - \frac{s}{\gamma_d}\right), \tag{32}$$

and comparing it directly with the expansion of $\tilde{Q}(s)$ in equation (23). First we expand $f(s)$ into a Taylor series with respect to s, i.e.

$$f(s) = q_1\kappa - (q_1/\gamma_{01})\beta s + \left(q_1/\gamma_{01}^2\right)\delta s^2 + O(s^3) \tag{33}$$

with the coefficients

$$\begin{aligned} \kappa &= 1/q_1 + 1 + q_2 \\ \beta &\equiv (1 + q_2)^2 + q_2 q_4 \\ \delta &\equiv (1 + q_2)^3 + 2q_2 q_4(1 + q_2) + q_2 q_4^2, \end{aligned} \tag{34}$$

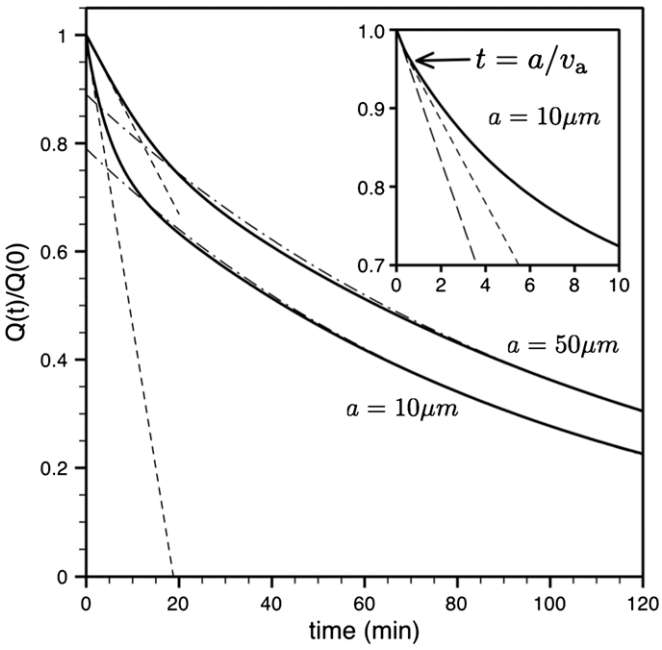

Figure 5. Comparison of the relative fluorescence decay $Q(t)/Q(0)$ in our model with the approximations for small and large times for two different lengths of activation window, i.e. $a = 10$ μm (bottom) and $a = 50$ μm (top). The dashed lines indicate the approximations (equation (29)) for small times and the dashed–dotted lines indicate the approximations (equation (31)) for large times. The inset shows the initial fluorescent decay for the 10 μm window at small times together with the short time approximations for $t < a/v_a$ (long-dashed lines) and for $t > a/v_a$ (short-dashed line) (equation (29)). The arrow points to the cusp point at $t = a/v_a$. The rate constants are $\gamma_{01} = 0.005$ s^{-1}, $\gamma_{10} = 0.05$ s^{-1}, $\gamma_{\mathrm{on}} = 2 \times 10^{-4}$ s^{-1} and $\gamma_{\mathrm{off}} = 5 \times 10^{-4}$ s^{-1}.

and $q_4 = \gamma_{01}/\gamma_{\mathrm{on}}$. Then we expand equation (23) for small s and utilize equations (33) and (34) to obtain

$$\begin{aligned} \tilde{Q}(s) &= A - Bs + o(s^2) = A\left(1 - \frac{B}{A}s\right) + o(s^2) \\ &= A\left(1 - \frac{s}{\gamma_d}\right) + o(s^2) \end{aligned} \tag{35}$$

with

$$\begin{aligned} A &= \frac{a\rho\eta q_1}{\gamma_{01}}\left(\beta(1 + q_3) + \frac{1}{2}\kappa^2\varepsilon\left(1 - q_3\frac{v_a}{v_r}\right)\right) \\ B &= \frac{a\rho\eta q_1}{\gamma_{01}^2}\left(\delta(1 + q_3) + \kappa\beta\varepsilon\left(1 - q_3\frac{v_a}{v_r}\right)\right. \\ &\quad \left. + \frac{1}{6}\kappa^3\varepsilon^2\left(1 + q_3\left(\frac{v_a}{v_r}\right)^2\right)\right) \end{aligned} \tag{36}$$

and

$$\varepsilon = \frac{a\gamma_{10}}{v_a}. \tag{37}$$

Comparing with equation (32), we find for the asymptotic pulse-escape decay exponent

$$\gamma_d = \gamma_{01}\frac{\beta + \frac{1}{2}\frac{\kappa^2}{1+q_3}\varepsilon\left(1 - q_3\frac{v_a}{v_r}\right)}{\delta + \frac{\kappa\beta}{1+q_3}\varepsilon\left(1 - q_3\frac{v_a}{v_r}\right) + \frac{1}{6}\frac{\kappa^3}{1+q_3}\varepsilon^2\left(1 + q_3\left(\frac{v_a}{v_r}\right)^2\right)}. \tag{38}$$

and

$$Q_\infty = \frac{A^2}{B} = A\gamma_d.$$

For small activation windows, i.e. $a \ll v_a/\gamma_{10}$ and $a \ll |v_r|/\gamma_{10}$ or equivalently $\varepsilon_a, |\varepsilon_r| \ll 1$, the decay exponent becomes independent of the size of the activation window, i.e.

$$\gamma_d \approx \gamma_{01}\frac{\beta}{\delta}, \tag{39}$$

which coincides with the smallest pole of $f(s)$ given by equation (24) and is directly related to the inverse average pause time of the neurofilaments (see [14]). In this limit of small window sizes, the exponential decay of fluorescence probes directly the pausing kinetics of neurofilaments because neurofilaments that switch into the moving states escape the activation window without cycling back into pausing states. If the window sizes are larger, i.e. $\varepsilon_{a,r}$ are not small, neurofilaments in the mobile states may switch back into a pausing state before leaving the activation window, and this gives rise to a dependence of the decay exponent on the size of the activation window that is described by the dependence of equation (38) on ε.

As noted above for the decay at short times (see equation (29)), the reversal rate ratio q_3 enters into equation (38) for the decay exponent γ_d (even though we neglect reversals) because this ratio determines the relative proportion of neurofilaments in the anterogradely and retrogradely moving states. In the special case of equal anterograde and retrograde speeds, i.e. $v_r = -v_a$, the dependence on the reversal rates disappears, i.e.

$$\gamma_d = \gamma_{01}\frac{\beta + \frac{1}{2}\varepsilon\kappa^2}{\delta + \kappa\beta\varepsilon + \frac{1}{6}\kappa^3\varepsilon^2}$$

$$Q_\infty = \frac{a\rho}{\kappa}\frac{\left(\beta + \frac{1}{2}\kappa^2\varepsilon\right)^2}{\delta + \kappa\beta\varepsilon + \frac{1}{6}\kappa^3\varepsilon^2}. \tag{40}$$

In figure 5 we compare the numerical solutions of equations (1)–(6) with the large-time approximation in equation (31). The exponent γ_d and the prefactor Q_∞ both agree well with the numerical solutions for two different window sizes.

Note that the length a of the activation window enters into the above expressions for the long-term decay, as it did for the short-term decay, through the parameter $\varepsilon = a\gamma_{10}/v_a$. For example, figure 6 shows the simulated pulse-escape decay kinetics for four different activation window sizes. For any given set of rate constants, the decay kinetics are faster at both short and long times for shorter activation windows. This has important practical implications for the design and interpretation of pulse-escape experiments, particularly when comparing pulse-escape kinetics in different axons or at different locations along the same axon (see section 7).

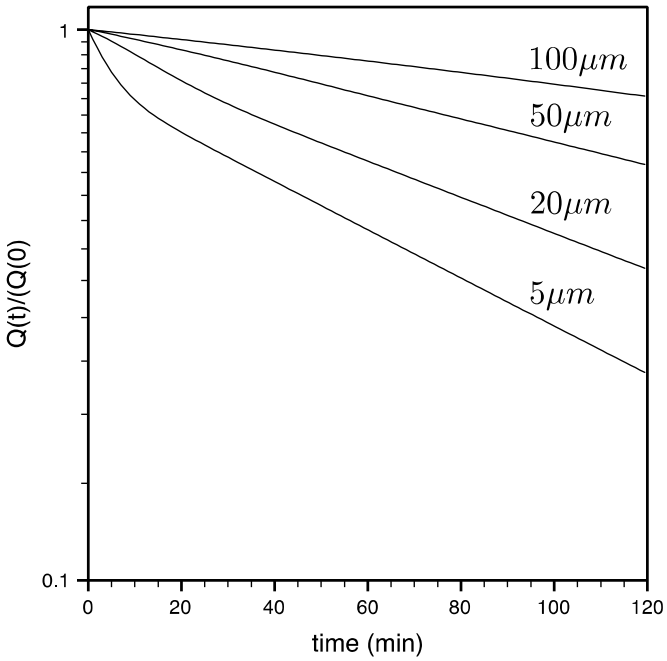

Figure 6. Influence of the window size on the decay kinetics. The relative fluorescence decay $Q(t)/Q(0)$ is shown for four different window sizes with $\gamma_{01} = 0.01\ \text{s}^{-1}$, $\gamma_{10} = 0.4\ \text{s}^{-1}$, $\gamma_{\text{on}} = 2 \times 10^{-4}\ \text{s}^{-1}$ and $\gamma_{\text{off}} = 5 \times 10^{-4}\ \text{s}^{-1}$. Note that not only the initial slope decreases with increasing window size, as predicted by equation (28), but also the time-constant of the long-term exponential decay.

5. Results

The analysis above now permits us to extract kinetic rate constants of neurofilament transport from fluorescence photoactivation pulse-escape experiments. To demonstrate this, we use the published experimental data shown in figure 3 for axons of cultured neurons from rat SCG and mouse DRG [11, 24]. These data show the decline in the fluorescence of the activation window over a 2 h period ($Q(t)$), normalized to the fluorescence at $t = 0$, immediately after activation ($Q(0)$). Published measurements of the average velocities of neurofilament movement have ranged from 0.38 to 0.53 μm s^{-1} for v_a and from -0.49 to -0.60 μm s^{-1} for v_r [8, 9, 24, 25, 27]. For the purposes of this analysis, we assume $v_a = 0.5$ μm s^{-1} and $v_r = -0.5$ μm s^{-1}. As described earlier, the experimental data are fitted well by a double exponential function, which allows us to read off the initial slope α and the time constant of the exponential decay γ_d for long times. As a result, the four rate constants γ_{01}, γ_{10}, γ_{on} and γ_{off} are constrained by the two equations (29) and (40), leaving us with two independent rate constants (we chose γ_{01} and γ_{10}). These rate constants are then determined by fitting the numerical solutions of our model to the experimental data. Specifically, we compute the pulse-escape decay curves for all possible combinations of γ_{01} and γ_{10} and determine the least square error of the computed curves with respect to the experimental data. Finally, we optimize the fit at longer times by repeating this procedure for slightly perturbed values of γ_d. The approach of using asymptotic expansions of solutions of partial differential equations to extract parameters through comparison with experiments has also been utilized in [28].

For the pulse-escape data shown in figure 3, the double exponential fits to the data deliver $\alpha = A_1/\tau_1 + A_2/\tau_2 = 3.50 \times 10^{-4}\ \text{s}^{-1}$, and $\gamma_d = 1/\tau_1 = 1.5 \times 10^{-4}\ \text{s}^{-1}$ for the SCG neurons, and $\alpha = A_1/\tau_1 + A_2/\tau_2 = 4.20 \times 10^{-4}\ \text{s}^{-1}$, and $\gamma_d = 1/\tau_1 = 2.97 \times 10^{-5}\ \text{s}^{-1}$ for the DRG neurons.

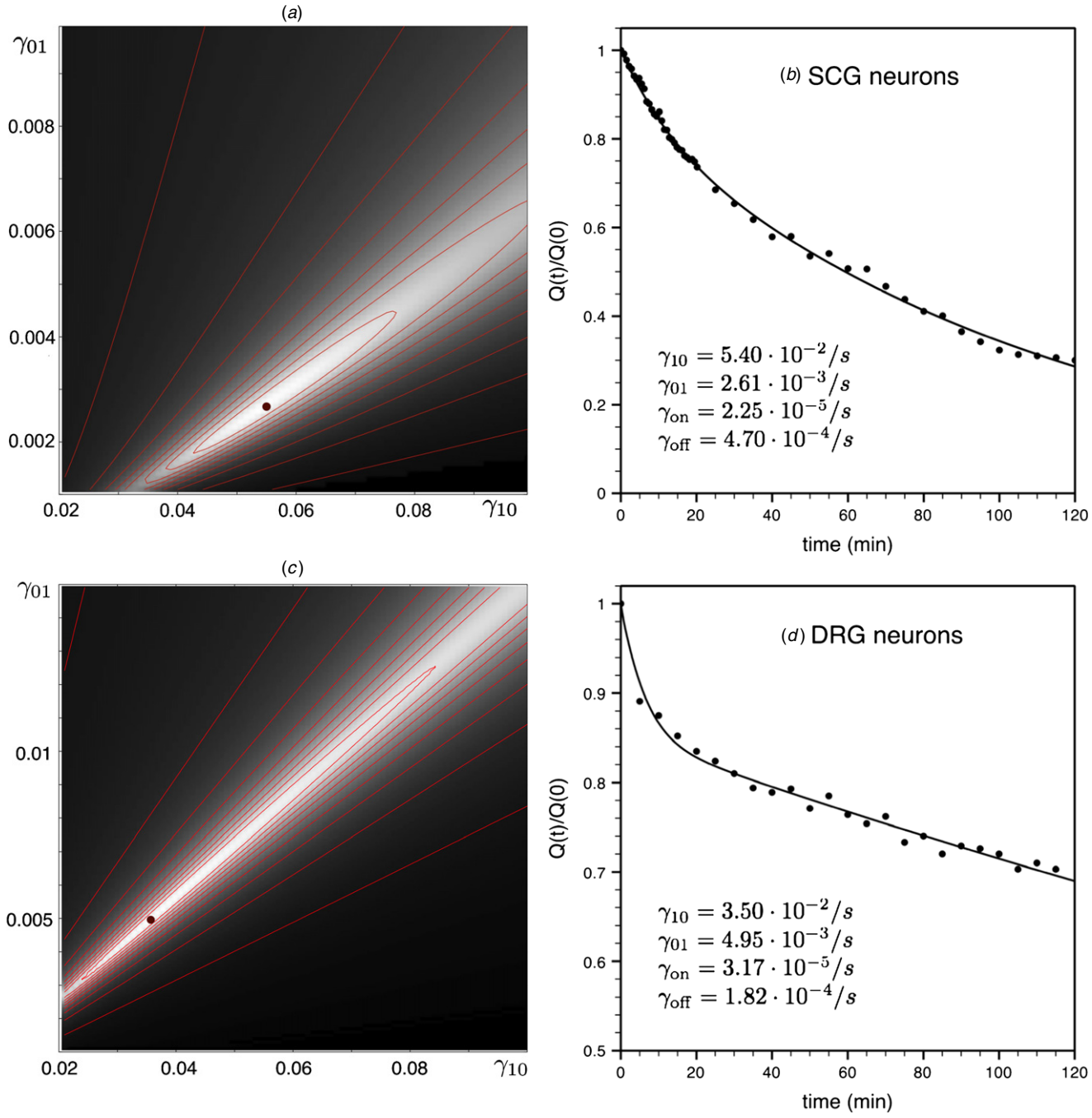

Figure 7. Fitting the experimental data. The contour plots (*a*) and (*c*) show the goodness of fit of the model to the pulse-escape data in the two dimensional parameter space γ_{01}, γ_{10} for the SCG and DRG neurons respectively. For each combination of values for the rate constants γ_{01} and γ_{10}, the other two rate constants γ_{on} and γ_{off} were adjusted to obtain the best match to the initial slope and the long-term exponential decay using our analytical approximations for short and long times (see equations (29) and (31)). Then we simulated the decay kinetics using those parameter values and estimated the goodness of fit to the experimental data using a least squares method. This was repeated for all combinations of γ_{01} and γ_{10} in the parameter space and the goodness of fit was plotted with a gray scale lookup table where the lighter the color, the better the fit. The red lines represent the contour lines of equal error, and the red spots indicate the points of least error, which correspond to the optimal values for γ_{01} and γ_{10}. The graphs in (*b*) and (*d*) compare simulations of the relative fluorescence decay $Q(t)/Q(0)$ (performed with the optimized rate constants) to the experimental decay kinetics for the SCG and DRG neurons, respectively.

Figures 7(*a*) and (*c*) show contour plots of the inverse error in the γ_{10}–γ_{01} plane, where lighter gray indicates a smaller error. For each data set, we find a single peak in the contour plot, which corresponds to the optimum set of values for γ_{01} and γ_{10}. Repeating the procedure for with slightly perturbed values of γ_d yields a minimum error for $\gamma_d = 1/\tau_1 = 1.60 \times 10^{-4}$ s^{-1} for the SCG neurons but no decrease in the error for the DRG neurons, confirming that $\gamma_d = 1/\tau_1 = 2.97 \times 10^{-5}$ s^{-1} was the best fit. In figures 7(*b*) and (*d*), we compare the resulting optimal computed decay curves with the experimental data.

Table 1 shows the computed kinetic rate constants based on the optimized numerical solutions shown in figure 7.

Table 1. Comparison of the extracted rate constants for the SCG and DRG neurons and the predicted kinetic features of neurofilament transport in these cells. The rate constants γ_{01}, γ_{10}, γ_{on}, γ_{off} are defined in figure 1. $\langle T_{on}\rangle$ and $\langle T_{off}\rangle$ represent the average duration of time that the filaments spend on- and off-track, respectively [14]. The fractions of off-track and on-track neurofilaments are given by $f_{off} = (\rho_{ap} + \rho_{rp})/\rho$ and $f_{on} = (\rho_a + \rho_{a0} + \rho_r + \rho_{r0})/\rho$ respectively (see equations (10), (11)). The fraction of on-track moving neurofilaments is given by $f_{run} = (\rho_a + \rho_r)/\rho$.

Rates	SCG neurons	DRG neurons
γ_{01} (s^{-1})	2.29×10^{-3}	4.80×10^{-3}
γ_{10} (s^{-1})	4.70×10^{-2}	3.40×10^{-2}
γ_{on} (s^{-1})	2.34×10^{-4}	3.17×10^{-5}
γ_{off} (s^{-1})	4.95×10^{-4}	1.81×10^{-4}
$\langle T_{on}\rangle$ (min)	5.98	3.35
$\langle T_{off}\rangle$ (min)	71.2	526
f_{off} (%)	66.9	83.3
f_{on} (%)	33.1	16.7
f_{run} (%)	1.54	2.06

Knowing these kinetic rate constants, we can characterize the pausing behavior. The rate constant γ_{on} was approximately seven times smaller for the DRG neurons and the rate constant γ_{off} was approximately three times smaller. The rate constants γ_{01} and γ_{10} were approximately 2 times larger and 1.4 times smaller, respectively. Consequently, the average off-track pause time given by $\langle T_{off}\rangle = 1/\gamma_{on}$ [14] was 526 min for the DRG neurons versus 71.2 min for the SCG neurons, and the average on-track pause time given by $\langle T_{on}\rangle = 1/(\gamma_{01}+\gamma_{off})$ [14] was 3.4 min for the DRG neurons versus 6 min for the SCG neurons. Thus neurofilaments in the DRG neurons exhibit longer off-track pauses and shorter on-track pauses. The average time of all pauses (both on- and off-track) is given by [14]

$$\langle T\rangle = \frac{1}{\lambda_-} - \frac{\gamma_{01} - \lambda_-}{\lambda_-\lambda_+} \tag{41}$$

with

$$\lambda_\pm = \tfrac{1}{2}(\gamma_{01} + \gamma_{on} + \gamma_{off}) \mp \tfrac{1}{2}\sqrt{(\gamma_{01} + \gamma_{on} + \gamma_{off})^2 - 4\gamma_{01}\gamma_{on}} \tag{42}$$

and is similar for both neuronal cell types, i.e. 22.6 min for the SCG neurons versus 23.3 min for DRG neurons.

To calculate the net average velocity of neurofilament transport we need to know the balance of anterograde and retrograde movements, which are dictated by the reversal rate constants γ_{ar} and γ_{ra}. Since the pulse-escape experiments are blind to the direction in which the neurofilaments leave the activation window, we cannot determine the reversal rate constants using this method (see above). However, we can extract the average transport velocity up to the factor $(1 + q_3)/(1 - q_3)$, where q_3 is the ratio of the reversal rates γ_{ar}/γ_{ra} (see equation (30)).

Using equation (7), we can see that this ratio is identical to the fraction of anterogradely and retrogradely moving neurofilaments, i.e.

$$\frac{\rho_a + \rho_{a0} + \rho_{ap}}{\rho_r + \rho_{r0} + \rho_{rp}} = \frac{1}{q_3} = \frac{\gamma_{ra}}{\gamma_{ar}}, \tag{43}$$

which has been determined using single-neurofilament tracking experiments to be $q_3 = 31/69 = 0.450$ for rat SCG neurons [9, 14]. Hence for these neurons we find

$$\bar{v}_{SCG} = \alpha a \frac{1 - q_3}{1 + q_3} = 0.252 \ \text{mm d}^{-1}. \tag{44}$$

Single-neurofilament tracking is not possible in DRG neurons due to their high neurofilament content and thus the relative proportion of anterogradely and retrogradely moving neurofilaments has not been determined in these cells. However, assuming the same ratio as for SCG neurons, we find

$$\bar{v}_{DRG} = \alpha a \frac{1 - q_3}{1 + q_3} = 0.337 \ \text{mm d}^{-1}. \tag{45}$$

6. Pulse-escape in the presence of diffusion

So far we have ignored diffusion because neurofilament proteins are almost fully assembled into neurofilament polymers in neurons and the polymers are too large to diffuse appreciably. Thus there is no loss of fluorescence from the activation window in pulse-escape experiments when neurofilament transport is inhibited [11]. However, the pulse-escape fluorescence photoactivation technique is also a potentially powerful method for studying the slow axonal transport of other cargoes for which this assumption may not hold. For example, variants of the pulse-escape technique have been used to study the slow axonal transport of cytosolic proteins, which can spend a proportion of their time in a diffusible state. The current model for the movement of these proteins is a biased diffusion in which transient and reversible associations of these proteins with motor-driven cargo complexes are superimposed on a backdrop of random diffusive motion, referred to as dynamic recruitment mechanism [29]. For such proteins, fluorescent photoactivation pulse-escape experiments result in diffusive spreading of the activated pool with an anterograde bias [30, 31]. Disabling the motors removes the anterograde bias, but not the diffusive spreading. The resulting model for the transport of cytosolic proteins is a combination rapid intermittent movement (similar to on-track neurofilaments) and passive diffusion.

To generalize our model so that it can also describe the transport of cytosolic proteins, we can adapt our six-state model for neurofilaments (figure 1) to allow for diffusion in the off-track state (see also [19]). According to this model, cytosolic proteins cycle between an on-track state in which they associate with motor-driven complexes or cargoes that exhibit rapid intermittent movement, and an off-track state in which they dissociate from these moving structures and become diffusible. Using this scheme, the equations now read (including reversal events)

$$\frac{\partial \rho_a}{\partial t} = -v_a \frac{\partial \rho_a}{\partial x} - \gamma_{10}\rho_a + \gamma_{01}\rho_{a0} \tag{46}$$

$$\frac{\partial \rho_{a0}}{\partial t} = -(\gamma_{01} + \gamma_{off} + \gamma_{ar})\rho_{a0} + \gamma_{10}\rho_a + \gamma_{on}\rho_{ap} + \gamma_{ra}\rho_{r0} \tag{47}$$

$$\frac{\partial \rho_{ap}}{\partial t} = -(\gamma_{on} + \gamma_{ar})\rho_{ap} + \gamma_{off}\rho_{a0} + \gamma_{ra}\rho_{rp} + D_0\frac{\partial^2 \rho_{ap}}{\partial x^2} \quad (48)$$

$$\frac{\partial \rho_r}{\partial t} = -v_r\frac{\partial \rho_r}{\partial x} - \gamma_{10}\rho_r + \gamma_{01}\rho_{r0} \quad (49)$$

$$\frac{\partial \rho_{r0}}{\partial t} = -(\gamma_{01} + \gamma_{off} + \gamma_{ra})\rho_{r0} + \gamma_{10}\rho_r + \gamma_{on}\rho_{rp} + \gamma_{ar}\rho_{a0} \quad (50)$$

$$\frac{\partial \rho_{rp}}{\partial t} = -(\gamma_{on} + \gamma_{ra})\rho_{rp} + \gamma_{off}\rho_{r0} + \gamma_{ar}\rho_{ap} + D_0\frac{\partial^2}{\partial x^2}\rho_{rp} \quad (51)$$

where D_0 is the diffusion coefficient of the transported molecules and x is distance along the axon. The effects of diffusion as described in equations (46)–(51) have also been studied earlier by Kuznetsov *et al* [32] using numerical solutions. Consistent with our analysis below, they observed the formation of Gaussian traveling waves at long times after initiation. As shown in [14, 17, 18], any pulse of labeled proteins that moves in a stochastic and intermittent manner will approach a Gaussian wave for large times, i.e.

$$\rho(x,t) = \frac{1}{\sqrt{2\pi Dt}}\exp\left(-\frac{(x-\bar{v}t)}{2Dt}\right), \quad (52)$$

with the average rate of movement $\bar{v}$ and the spreading rate D. Assuming that the pool of photoactivated proteins is in kinetic equilibrium, the average transport rate $\bar{v}$, defined through

$$\langle x(t)\rangle = \int_{-\infty}^{\infty} x(\rho_a(x,t) + \rho_{a0}(x,t) + \rho_{ap}(x,t) + \rho_r(x,t) + \rho_{r0}(x,t) + \rho_{rp}(x,t))\,\mathrm{d}x \quad (53)$$

and (with appropriate initial conditions) given by $\bar{v} = \langle x(t)\rangle/t$, is the same as in the case without diffusion because free diffusion has no directional bias. For the spreading rate D of the photoactivated proteins (relevant after a Gaussian wave has formed) we find two components: the spreading rate in the absence of diffusion and an additional term that is the product of the fraction of proteins in the off-track states and the diffusion coefficient D_0 in the off-track states, i.e. (see appendix B)

$$D = \frac{\mathrm{d}}{\mathrm{d}t}(\langle x^2\rangle - \langle x\rangle^2) = D_{kin} + 2D_0\frac{q_1q_2}{1+q_1(1+q_2)} \quad (54)$$

with

$$D_{kin} = \frac{2\bar{v}^2q_1}{1+q_1(1+q_2)}\left(\frac{q_2}{\gamma_{on}} + \frac{(1+q_2)^2}{\gamma_{01}}\right) + \frac{2\gamma_{ar}\gamma_{ra}}{\gamma_{rev}^2}\frac{1}{\gamma_{10}} \times \frac{1}{1+q_1(1+q_2)}\left(1+\frac{\gamma_{01}}{\gamma_{rev}}\frac{\gamma_{on}+\gamma_{rev}}{\gamma_{on}+\gamma_{off}+\gamma_{rev}}\right)(v_a-v_r)^2. \quad (55)$$

The coefficient D_{kin} in equation (55) describes the effective diffusive spreading due to random switching between the kinetic states (see also [17, 18]) at times when a Gaussian wave has formed, while the second term (which is proportional to D_0) describes the effects of diffusion of off-track proteins. Note that the latter contribution is proportional to the fraction of proteins in the off-track states $q_1q_2/(1+q_1(1+q_2))$.

According to this model, the predicted initial decay of the fluorescence in pulse-escape experiments is due predominantly to proteins in the off-track states diffusing out of the activation window. This is because the decay of the initial distributions (see equation (7)) of proteins in the activation window in their respective kinetic states due to transitions between those kinetic states is linear, whereas the diffusive decay follows the stronger time dependence $\propto t^{1/2}$. Solving the diffusion equation for the off-track proteins for small times (see appendix C) yields the following expression for the initial decay of the fluorescence

$$\frac{Q(t)}{Q(0)} = 1 - \frac{1}{a}\frac{(v_a - q_3v_r)}{(1+q_1(1+q_2))(1+q_3)}t - \frac{1}{a}\frac{2q_1q_2}{1+q_1(1+q_2)}\sqrt{\frac{D_0t}{\pi}}. \quad (56)$$

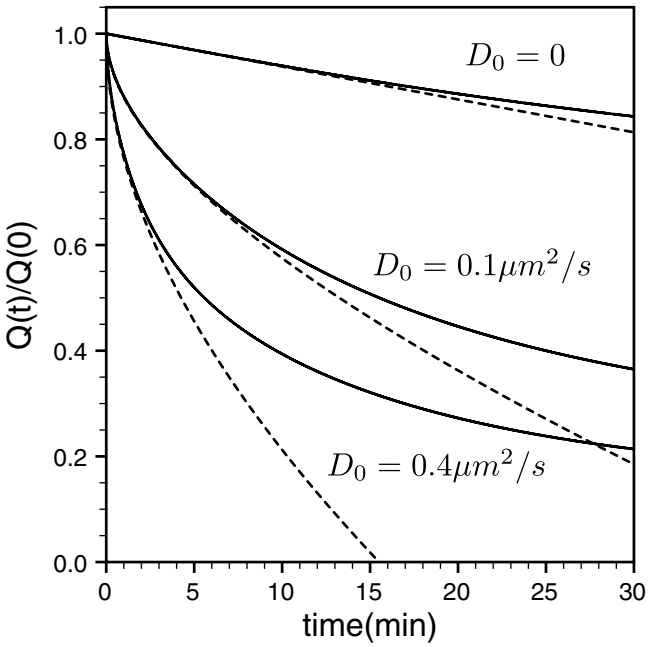

Figure 8. Simulation of a pulse-escape experiment for a cytosolic protein that is diffusible in the off-track state. The computed relative fluorescence decay $Q(t)/Q(0)$ is shown for three different diffusion coefficients, i.e. $D_0 = 0$ (no diffusion), $D_0 = 0.1$ μm^2 s^{-1} and $D_0 = 0.4$ μm^2 s^{-1}. The solid curves indicate numerical solutions, while the associated dashed lines indicate the analytical predictions based on equation (56). The rate constants are $\gamma_{10} = 0.1$ s^{-1}, $\gamma_{01} = 5.0\times10^{-3}$ s^{-1}, $\gamma_{on} = 1.0\times10^{-4}$ s^{-1} and $\gamma_{off} = 5.0\times10^{-4}$ s^{-1}.

The first term on the right-hand side describes the escape of proteins in the on-track state, while the second term describes the escape of proteins due to diffusion in the off-track state. In figure 8, we compare the analytical prediction for the initial fluorescent decay in equation (56) with numerical simulations and find good agreement. The significant qualitative difference in the decay kinetics in the presence of passive diffusion makes the pulse-escape method an excellent method to identify whether tracked objects exhibit passive diffusion.

7. Discussion

In this paper we have developed an analytical solution for the kinetics of neurofilament transport in fluorescent activation

pulse-escape experiments based on the kinetic parameters in a six-state kinetic model (see figure 1). According to this model, neurofilaments cycle between distinct mobile and immobile states during their transport along the axon. Neurofilaments in the mobile (on-track) state move in rapid bursts of anterograde or retrograde movement interrupted by short pauses that average seconds or minutes in duration whereas neurofilament in the immobile (off-track) state pause on average for an hour or more without movement. We found that the decay of fluorescence immediately after photoactivation is linear and proportional to the average transport velocity (including all movements and pauses), while the decay at longer times provides information predominantly about the transitions between the on and off-track pausing states. Utilizing the expressions that we obtained for the decay kinetics on short and long time scales, we have described a systematic computational method to extract from the experimental data optimal values for the rate constants in our model.

In our original description of the fluorescence photoactivation pulse-escape technique we performed stochastic simulations of pulse-escape experiments in rat SCG neurons, simulating on-track transitions with a transition probability matrix [11]. The transition probability matrix comprised seven distinct velocity states and was obtained directly from our single-neurofilament tracking data in the same neuronal cell type [13]. To estimate the values of γ_{on} and γ_{off} in our model, we varied the values of these rate constants systematically in order to match the experimental data. The best match was obtained for $\gamma_{on} = 0.000\,275\ s^{-1}$ and $\gamma_{off} = 0.004\,44\ s^{-1}$, which yielded predicted average pause times of $\langle T_{on}\rangle = 29$ s (on-track) and $\langle T_{off}\rangle = 61$ min (off-track) [11][3]. Subsequently we showed that the seven-state transition probability matrix that we used in those studies could be simplified to a matrix based on just two velocities (moving or pausing) and described by the rate constants $\gamma_{01} = 0.041\ s^{-1}$ and $\gamma_{10} = 0.093\ s^{-1}$ [14]. Importantly, however, our original transition probability matrix and this simpler matrix were both derived from the transitions measured in our single-neurofilament tracking experiments assuming that those kinetics represented the on-track kinetics, though in reality the on-track and off-track states are kinetically defined concepts and it is not possible to tell by looking at a single filament which of those states it is in at any point in time. In the analytical approach described in the present study we extract both the on- and off-track kinetics from the pulse-escape decay kinetics, eliminating the need to make this assumption. Moreover, our new computational method allows us to probe the parameter space more efficiently, ensuring that we obtain a single and unique optimum.

Using our new approach, we obtained revised estimates for the rate constants of neurofilament transport in SCG neurons of $\gamma_{01} = 0.002\,29\ s^{-1}$, $\gamma_{10} = 0.004\,70\ s^{-1}$, $\gamma_{on} = 0.000\,234\ s^{-1}$ and $\gamma_{off} = 0.000\,495\ s^{-1}$ (table 1). If we first consider the rate constants that govern the transitions between the on-track and off-track states, the revised estimate for γ_{on} is similar to our original estimate of $\gamma_{on} = 0.000\,275\ s^{-1}$, but the revised estimate for γ_{off} is lower than our original estimate of $\gamma_{off} = 0.004\,44\ s^{-1}$. This results in a ratio $\gamma_{on}/\gamma_{off} = (0.000\,234/0.000\,495) = 0.47$ that is about nine-fold higher than in our original estimates ($\gamma_{on}/\gamma_{off} = (0.000\,274/0.004\,44) = 0.062$). However, since the average time spent pausing off-track is dependent only on γ_{on}, our revised estimate of $\langle T_{off}\rangle = 1/\gamma_{on} = 71.2$ min agrees reasonably well with our original estimate of $\langle T_{off}\rangle = 61$ min. Turning next to the rate constants that govern the transitions between the on-track moving and pausing states, the ratio $\gamma_{01}/\gamma_{10} = (0.002\,29/0.0047) = 0.49$ in the revised analysis is similar to our original analysis ($\gamma_{01}/\gamma_{10} = (0.041/0.093) = 0.44$) but the absolute magnitude of these rate constants is about 20-fold lower. This suggests that our original analysis *overestimated* the frequency of the transitions between the on-track moving and pausing states and therefore *underestimated* the durations of the on-track movements and pauses. Based on our revised estimates for γ_{01} and γ_{off}, we obtained a revised estimate of the average on-track pause time of $\langle T_{on}\rangle = 1/(\gamma_{01} + \gamma_{off}) = 5.98$ min, which is about 12 times longer than our original estimate $\langle T_{on}\rangle = 29$ s. Overall these revised analyses predict that the filaments spend an average of 33% of their time on-track (table 1) compared to only 8% of their time on-track in our previous analyses. Thus we conclude that single-neurofilament tracking experiments in naturally occurring or photobleached gaps do not capture the full extent of on-track neurofilament pausing and that the apparent discrepancy between our new and original estimates for the transport kinetics of neurofilaments in cultured rat SCG neurons can be explained because some of the pauses that we assumed originally off-track were actually on-track.

A limitation of the pulse-escape method is that it does not yield information on the reversal rate constants. This is because the method is blind to the direction of departure of the neurofilaments from the photoactivated regions. It may be possible to modify the pulse-escape method in future studies to address this limitation, but since the average velocity of neurofilament transport depends only on the ratio of anterograde and retrograde movements and not on the absolute magnitude of the reversal rate constants, it is still possible to estimate the average velocity of neurofilament transport in pulse-escape experiments if the velocity and relative proportion of anterogradely and retrogradely moving neurofilaments are known. In the case of the rat SCG neurons, we estimated the average velocity, including on- and off-track pauses, to be 0.25 mm d^{-1} (equation (44)). This is about a factor of two smaller than our original estimate of 0.5 mm d^{-1} [11], but it still falls within the 0.2–3 mm d^{-1} range obtained in radioactive pulse-labeling experiments on mature axons *in vivo* [33]. The explanation for the difference between our original and current estimates is that our current analysis predicts that the filaments spend 1.5% of their time moving (table 1), whereas our previous analysis estimated the moving fraction to be 3% [11].

An important advantage of our new analytical approach is that it can permit the characterization of neurofilament transport in mature axons for which single-neurofilament

[3] Note that the rate constants in the study of Trivedi *et al* [11] were expressed in units corresponding to the average time-lapse interval. The values quoted here are expressed in units of s^{-1}.

tracking is optically challenging due to the axon thickness or abundance of neurofilaments. For example, we recently used this approach to study neurofilament transport in long-term myelinating co-cultures of DRG neurons and Schwann cells [34]. Of course, it is important to note that the on- and off-track states in our model are kinetic concepts that presently have no physical correlates. As their names suggest, we have proposed that they may represent populations of neurofilaments that differ transiently in their proximity or engagement with microtubule tracks. However, experimental proof of this will require the identification of physical differences between these kinetic pools and experimental interventions to show that alterations in these pools have the expected effects on the decay kinetics.

To further explore the utility of our approach, we compared the pulse-escape kinetics in cultured rat SCG neurons with cultured mouse DRG neurons, which exhibit a biphasic decay profile with distinct kinetics [24]. A major difference between the decay kinetics of these neuronal cell types is in the proportion of the neurofilaments that remain in the activated regions on long time scales. For example, on average approximately 30% of the neurofilaments remained in the activated regions for the SCG neurons after 2 h, whereas approximately 70% remained for the DRG neurons. However, perhaps surprisingly, our analyses predict that the average velocity of neurofilament transport in the DRG neurons is 0.337 mm d^{-1} (equation (45)), which is 34% *faster* than in the SCG neurons. The reason for this is that while the slope of the decay kinetics in the DRG neurons is shallower at later times, it is steeper at early times, and we have shown that the initial slope is linearly related to the average velocity of neurofilament transport (equation (28)). This can be understood as follows. At the time of photoactivation, neurofilaments in the mobile states leave the activation window anterogradely and retrogradely proportional to their relative fraction. Once the mobile neurofilaments have left the activation window, the fraction of mobile (on-track) neurofilaments becomes smaller, leaving a larger fraction of immobile (off-track) neurofilaments behind. The departure time from the activation window is now determined by the time it takes for the neurofilaments to switch from the immobile states into the mobile states. Hence the overall slower decay of the fluorescent in the DRG neurons reflects longer dwell times in the off-track states, but not a slower average velocity. Specifically, our analyses predict that the average duration of off-track pausing in the DRG neurons is 526 min (more than 8 h), yet the average duration of on-track pausing is only 3.35 min. Overall the filaments spend 16.7% of their time on-track, which is about half the amount of time estimated for SCG neurons. Thus the picture that emerges for DRG neurons is that the neurofilaments spend more time pausing off-track but move more efficiently when they are on-track. The explanation for this difference is an interesting question, but answering it will require more understanding about the factors that regulate neurofilament transport in axons.

In addition to establishing a linear relationship between the initial slope in the pulse-escape decay kinetics and the average velocity, our analyses also reveal that the pulse-escape decay kinetics are very sensitive to the length of the activated region (figure 6). The explanation for this strong dependence is that the longer the activation window the higher the probability that on-track neurofilaments will transition to the off-track state before they exit the window. Together, these findings have important technical implications for the optimal design of pulse-escape experiments. First, it is important to ensure that the decay kinetics are sampled adequately at early times. Second, it is important to have an accurate measurement of the activation window. Combining these practical insights with the computational methods described in this paper, the fluorescence photoactivation pulse-escape technique represents a powerful complement to single-neurofilament tracking and radioisotopic pulse-labeling experiments for the analysis of neurofilament transport in axons.

Acknowledgments

This project was funded by collaborative NSF grants to AB and PJ and by a grant of the China Scholarship Council to YL. The authors declare that they have no competing financial interests.

Appendix A

In general, if the Laplace transform of a function $f(t)$ with a Taylor expansion at $t = 0$ of

$$f(t) = \sum_{n=0}^{\infty} \frac{f^{(n)}(0)}{n!} t^n, \tag{A.1}$$

where $f^{(n)}(0)$ denotes the nth derivative of $f(t)$ at $t = 0$, is given by $g(s)$ (assuming it exists), i.e.

$$g(s) = \int_0^{\infty} f(t)\, \mathrm{e}^{-st}\, \mathrm{d}t, \tag{A.2}$$

we can see by inserting equation (A.1) into (A.2) and subsequent term-by-term integration that

$$g(s) = \sum_{n=0}^{\infty} f^{(n)}(0)(-1)^n \frac{1}{s^{n+1}}. \tag{A.3}$$

Hence, the derivatives $f^{(n)}(0)$ can be obtained as the coefficients of the expansion of $g(s)$ in terms of $1/s$.

In our specific problem we first expand the function $f(s)$ given in equation (24) into a Taylor expansion in powers of $1/s$, i.e.

$$f(s) \approx 1 + \frac{\gamma_{10}}{s} - \frac{\gamma_{10}\gamma_{01}}{s^2} + \frac{\gamma_{10}\gamma_{01}(\gamma_{01} + \gamma_{\mathrm{off}})}{s^3} \tag{A.4}$$

and then insert equation (A.4) into (23) to find the following expression after subsequent Taylor expansion

$$\begin{aligned}\tilde{Q}(s) = {} & \frac{a\rho}{s} - \frac{\eta\rho(v_a - v_r q_3)}{s^2} + \exp(-\varepsilon_a)\frac{v_a\eta\rho}{s^2} \\ & \times \exp(-s\varepsilon_a/\gamma_{10}) - \exp(\varepsilon_r)\frac{v_r q_3 \eta\rho}{s^2}\exp(s\varepsilon_r/\gamma_{10}) \\ & + \exp(-\varepsilon_a)\frac{v_a\eta\rho\varepsilon_a\gamma_{01}}{s^3}\exp(-s\varepsilon_a/\gamma_{10}) \\ & + \exp(\varepsilon_r)\frac{v_r q_3\eta\rho\varepsilon_r\gamma_{01}}{s^3}\exp(s\varepsilon_r/\gamma_{10}) + O(s^{-4})\end{aligned} \tag{A.5}$$

with ε_a and ε_r defined in equation (26).

Using the following rules for the Laplace transformation

$$\begin{aligned} &1/s \leftrightarrow 1 \\ &1/s^2 \leftrightarrow t \\ &1/s^2 \exp(-\alpha s) \leftrightarrow (t-\alpha)\Theta(t-\alpha) \\ &1/s^3 \leftrightarrow (1/2)t^2 \\ &1/s^3 \exp(-\alpha s) \leftrightarrow (1/2)(t-\alpha)^2\Theta(t-\alpha) \end{aligned} \quad , \tag{A.6}$$

we find (25) for the neurofilament content in the activation window at short times.

Appendix B

The mean rate of movement is found from equations (46)–(51) by deriving the equation of motions for the moment (53), i.e.

$$\frac{\mathrm{d}}{\mathrm{d}t}\langle x\rangle = \int_{-\infty}^{\infty}\Big(- v_a\frac{\partial}{\partial x}\rho_a(x,t) - v_r\frac{\partial}{\partial x}\rho_r(x,t) + D_0\frac{\partial^2}{\partial x^2}\rho_{\mathrm{ap}}(x,t) + D_0\frac{\partial^2}{\partial x^2}\rho_{\mathrm{rp}}(x,t)\Big)\,\mathrm{d}x. \tag{B.1}$$

Integrating the third and the fourth term on the right-hand side of (B.1) in parts and using the natural boundary conditions we find

$$\frac{\mathrm{d}}{\mathrm{d}t}\langle x\rangle = v_a p_a + v_r p_r \tag{B.2}$$

with

$$p_{\dots} \equiv \int_{-\infty}^{\infty}\rho_{\dots}(x,t)\,\mathrm{d}x. \tag{B.3}$$

It is straightforward to set up the equations of motion for p_a and p_r, i.e.

$$\begin{aligned} \dot{p}_a &= -\gamma_{10}p_a + \gamma_{01}p_{a0} \\ \dot{p}_r &= -\gamma_{10}p_r + \gamma_{01}p_{r0} \\ \dot{p}_{a0} &= -(\gamma_{01}+\gamma_{\mathrm{off}}+\gamma_{\mathrm{ar}})p_{a0} + \gamma_{10}p_a + \gamma_{\mathrm{on}}p_{\mathrm{ap}} + \gamma_{\mathrm{ra}}p_{r0} \\ \dot{p}_{r0} &= -(\gamma_{01}+\gamma_{\mathrm{off}}+\gamma_{\mathrm{ra}})p_{r0} + \gamma_{10}p_r + \gamma_{\mathrm{on}}p_{\mathrm{rp}} + \gamma_{\mathrm{ar}}p_{a0} \\ \dot{p}_{\mathrm{ap}} &= -(\gamma_{\mathrm{on}}+\gamma_{\mathrm{ar}})p_{\mathrm{ap}} + \gamma_{\mathrm{off}}p_{a0} + \gamma_{\mathrm{ra}}p_{\mathrm{rp}} \\ \dot{p}_{\mathrm{rp}} &= -(\gamma_{\mathrm{on}}+\gamma_{\mathrm{ra}})p_{\mathrm{rp}} + \gamma_{\mathrm{off}}p_{r0} + \gamma_{\mathrm{ar}}p_{\mathrm{ap}}. \end{aligned} \tag{B.4}$$

The diffusion terms in equation (B.1) do not contribute in equation (B.4) because of the natural boundary conditions. The stationary solutions of (B.4) are identical to the solutions given in (7). Since the closed set of equations in (B.2) and (B.4) do not contain the diffusion coefficient D_0 their solutions are the same as in the absence of diffusion (see [14]) and are given by

$$\langle x\rangle = \bar{v}t = \frac{1}{(1+q_1(1+q_2))(\gamma_{\mathrm{ar}}+\gamma_{\mathrm{ra}})}(\gamma_{\mathrm{ra}}v_a + \gamma_{\mathrm{ar}}v_r) \tag{B.5}$$

(see equation (27)).

For the spreading rate we follow the same strategy, i.e. setting up equations for motion

$$\frac{\mathrm{d}}{\mathrm{d}t}(\langle x^2\rangle - \langle x\rangle^2) = \int_{-\infty}^{\infty}x^2\Big(-v_a\frac{\partial}{\partial x}\rho_a(x,t) - v_r\frac{\partial}{\partial x}\rho_r(x,t) + D_0\frac{\partial^2}{\partial x^2}\rho_{\mathrm{ap}}(x,t) + D_0\frac{\partial^2}{\partial x^2}\rho_{\mathrm{rp}}(x,t)\Big) - 2\langle x\rangle\frac{\mathrm{d}}{\mathrm{d}t}\langle x\rangle. \tag{B.6}$$

The first term on the right-hand side of (B.6) is integrated by parts and in the second term we use (B.5) yielding

$$\frac{\mathrm{d}}{\mathrm{d}t}(\langle x^2\rangle - \langle x\rangle^2) = 2v_aM_a(t) + 2v_rM_r(t) - 2\bar{v}^2t + 2D_0(p_{\mathrm{ap}}(t) + p_{\mathrm{rp}}(t)), \tag{B.7}$$

with

$$M_{\dots}(t) = \int_{-\infty}^{\infty}x\rho_{\dots}(x,t)\,\mathrm{d}x.$$

Setting up equations of motion for $M_{\dots}$ one finds after integration in parts (as in the case without diffusion [14])

$$\begin{aligned} \dot{M}_a &= v_ap_a - \gamma_{10}M_a + \gamma_{01}M_{a0} \\ \dot{M}_r &= v_rp_r - \gamma_{10}M_r + \gamma_{01}M_{r0} \\ \dot{M}_{a0} &= -(\gamma_{01}+\gamma_{\mathrm{ar}}+\gamma_{\mathrm{off}})M_{a0} + \gamma_{10}M_a + \gamma_{\mathrm{ra}}M_{r0} + \gamma_{\mathrm{on}}M_{\mathrm{ap}} \\ \dot{M}_{r0} &= -(\gamma_{01}+\gamma_{\mathrm{ra}}+\gamma_{\mathrm{off}})M_{r0} + \gamma_{10}M_r + \gamma_{\mathrm{ar}}M_{a0} + \gamma_{\mathrm{on}}M_{\mathrm{rp}} \\ \dot{M}_{\mathrm{ap}} &= -(\gamma_{\mathrm{ar}}+\gamma_{\mathrm{on}})M_{\mathrm{ap}} + \gamma_{\mathrm{off}}M_{a0} + \gamma_{\mathrm{ra}}M_{\mathrm{rp}} \\ \dot{M}_{\mathrm{ap}} &= -(\gamma_{\mathrm{ra}}+\gamma_{\mathrm{on}})M_{\mathrm{ap}} + \gamma_{\mathrm{off}}M_{r0} + \gamma_{\mathrm{ar}}M_{\mathrm{rp}}. \end{aligned} \tag{B.8}$$

The solution of (B.8) is described in detail in the appendix of [14]. In the long-time limit we can replace $p_{\mathrm{ap}}(t)$ and $p_{\mathrm{rp}}(t)$ by their stationary (normalized) solutions (see (27)), i.e.

$$p_{\mathrm{ap}} + p_{\mathrm{rp}} = \frac{q_1q_2 + q_1q_2q_3}{(1+q_1(1+q_2))(1+q_3)} = \frac{q_1q_2}{(1+q_1(1+q_2))}$$

yielding for the spreading rate (B.7)

$$\frac{\mathrm{d}}{\mathrm{d}t}(\langle x^2\rangle - \langle x\rangle^2) = D_{\mathrm{kin}} + 2D_0\frac{q_1q_2}{1+q_1(1+q_2)} \tag{B.9}$$

with

$$D_{\mathrm{kin}} = \frac{2\bar{v}^2q_1}{1+q_1(1+q_2)}\left(\frac{q_2}{\gamma_{\mathrm{on}}} + \frac{(1+q_2)^2}{\gamma_{01}}\right) + \frac{2\gamma_{\mathrm{ar}}\gamma_{\mathrm{ra}}}{\gamma_{\mathrm{rev}}^2}\frac{1}{\gamma_{10}} \times \frac{1}{1+q_1(1+q_2)}\left(1 + \frac{\gamma_{01}}{\gamma_{\mathrm{rev}}}\frac{\gamma_{\mathrm{on}}+\gamma_{\mathrm{rev}}}{\gamma_{\mathrm{on}}+\gamma_{\mathrm{off}}+\gamma_{\mathrm{rev}}}\right)(v_a - v_r)^2, \tag{B.10}$$

Appendix C

The fraction of cytosolic proteins that are initially off-track, i.e. $(\rho_{\mathrm{ap}} + \rho_{\mathrm{rp}})/\rho = q_1q_2/(1+q_1(1+q_2))$ (see equation (7)), and that can escape the activation window $(0, a)$ by diffusion, is described by

$$\frac{\partial\rho_{\mathrm{off}}(x,t)}{\partial t} = D_0\frac{\partial^2\rho_{\mathrm{off}}(x,t)}{\partial x^2} \tag{C.1}$$

where D_0 is the diffusion coefficient and,

$$\rho_{\mathrm{off}}(x,t) = \rho_{\mathrm{ap}}(x,t) + \rho_{\mathrm{rp}}(x,t)$$

with the initial conditions

$$\rho_{\mathrm{off}}(x,0) = \begin{cases} A_0 \equiv \dfrac{q_1q_2}{1+q_1(1+q_2)}\rho & \text{for} \quad 0 < x < a \\ 0 & \text{for} \quad \text{otherwise} \end{cases} \tag{C.2}$$

The solution of equation (C.1) can be found using the Green's function formalism, i.e.

$$\rho_{\mathrm{off}}(x,t) = \frac{A_0}{\sqrt{4\pi D_0t}}\int_0^a \mathrm{d}x_0\exp\left(-\frac{(x-x_0)^2}{4D_0t}\right)\mathrm{d}x_0 = \frac{A_0}{2}\left(\mathrm{erf}\left(\frac{x}{\sqrt{4D_0t}}\right) - \mathrm{erf}\left(\frac{x-a}{\sqrt{4D_0t}}\right)\right) \tag{C.3}$$

where $\mathrm{erf}(x)$ denotes the error-function, i.e.

$$\mathrm{erf}(x) \equiv \frac{2}{\sqrt{\pi}} \int_0^x \exp(-s^2)\, \mathrm{d}s. \tag{C.4}$$

The temporal derivative of $\rho_{\mathrm{off}}(x,t)$ can be obtained as

$$\frac{\partial \rho_{\mathrm{off}}(x,t)}{\partial t} = \frac{A_0}{2}\sqrt{\frac{D}{\pi}}t^{-1/2}\frac{\partial}{\partial x}\left(\exp\left(-\frac{x^2}{4D_0t}\right)\right.$$

$$\left. - \exp\left(-\frac{(x-a)^2}{4D_0t}\right)\right) \tag{C.5}$$

which is then integrated over the window size to obtain the temporal derivative of the content due to diffusion, i.e.

$$\frac{\mathrm{d}Q_{\mathrm{off}}}{\mathrm{d}t} = \int_0^a \frac{\partial \rho_{\mathrm{off}}(x,t)}{\partial t}\mathrm{d}x$$

$$= -A_0\sqrt{\frac{D_0}{\pi}}t^{-1/2}\left(1 - \exp\left(-\frac{a^2}{4Dt}\right)\right). \tag{C.6}$$

For small times t, we neglect the exponential term and find

$$Q_{\mathrm{off}}(t) = Q_{\mathrm{off}}(0) - 2A_0\sqrt{\frac{D_0t}{\pi}}. \tag{C.7}$$

Combining the linear decay of fluorescence due to the movement of on-track proteins (see equation (25)) with the decay of fluorescence due to escape of diffusing off-track proteins we find

$$Q(t) = a\rho - \eta\rho(v_a - q_3v_r)t - 2\rho\frac{q_1q_2}{1+q_1(1+q_2)}\sqrt{\frac{D_0t}{\pi}}, \tag{C.8}$$

with ρ given in equation (9). Normalizing the initial fluorescence to unity, we obtain

$$\frac{Q(t)}{Q(0)} = 1 - \frac{1}{a}\frac{(v_a - q_3v_r)}{(1+q_1(1+q_2))(1+q_3)}t$$

$$-\frac{1}{a}\frac{2q_1q_2}{1+q_1(1+q_2)}\sqrt{\frac{D_0t}{\pi}}, \tag{C.9}$$

i.e. equation (56).

References

[1] Brown A 2009 Slow axonal transport *New Encyclopedia of Neuroscience* vol 9 ed L A Squire (Oxford: Academic) pp 1–9

[2] Lasek R J, Garner J A and Brady S T 1984 Axonal transport of the cytoplasmic matrix *J. Cell Biol.* **99** 212s–221s

[3] Brown A 2000 Slow axonal transport: stop and go traffic in the axon *Nature Rev. Mol. Cell Biol.* **1** 153–6

[4] Shah J V and Cleveland D W 2002 Slow axonal transport: fast motors in the slow lane *Curr. Opin. Cell Biol.* **14** 58–62

[5] Brown A 2003 Axonal transport of membranous and nonmembranous cargoes: a unified perspective *J. Cell Biol.* **160** 817–21

[6] Brown A and Jung P 2013 A critical reevaluation of the stationary axonal cytoskeleton hypothesis *Cytoskeleton (Hoboken)* **70** 1–11

[7] Brown A 2003 Live-cell imaging of slow axonal transport in cultured neurons *Methods Cell Biol.* **71** 305–23

[8] Wang L, Ho C L, Sun D, Liem R K and Brown A 2000 Rapid movement of axonal neurofilaments interrupted by prolonged pauses *Nature Cell Biol.* **2** 137–41

[9] Wang L and Brown A 2001 Rapid intermittent movement of axonal neurofilaments observed by fluorescence photobleaching *Mol. Biol. Cell* **12** 3257–67

[10] Wang L and Brown A 2010 A hereditary spastic paraplegia mutation in kinesin-1A/KIF5A disrupts neurofilament transport *Mol. Neurodegenertion* **5** 52

[11] Trivedi N, Jung P and Brown A 2007 Neurofilaments switch between distinct mobile and stationary states during their transport along axons *J. Neurosci.* **27** 507–16

[12] Blum J J and Reed M C 1989 A model for slow axonal transport and its application to neurofilamentous neuropathies *Cell Motil. Cytoskeleton* **12** 53–65

[13] Brown A, Wang L and Jung P 2005 Stochastic simulation of neurofilament transport in axons: the 'stop-and-go' hypothesis *Mol. Biol. Cell* **16** 4243–55

[14] Jung P and Brown A 2009 Modeling the slowing of neurofilament transport along the mouse sciatic nerve *Phys. Biol.* **6** 046002

[15] Craciun G, Brown A and Friedman A 2005 A dynamical systems model of neurofilament transport in axons *J. Theor. Biol.* **22** 316–22

[16] Reed M and Blum J 1985 A model for fast axonal transport *J. Cell Motil.* **5** 507–27

[17] Friedman A and Craciun G 2006 Approximate traveling waves in linear reaction-hyperbolic equations *SIAM J. Math. Anal.* **38** 741–58

[18] Reed M C, Venakides S and Blum J J 1990 Approximate traveling waves in linear reaction-hyperbolic equations *SIAM J. Appl. Math.* **50** 167–80

[19] Friedman A and Craciun G 2005 A model of intracellular transport of particles in an axon *J. Math. Biol.* **51** 217–46

[20] Popovic L, McKinley S A and Reed M C 2011 A stochastic compartmental model for fast axonal transport *SIAM J. Appl. Math.* **71** 1532–56

[21] Newby J M and Bressloff P C 2010 Quasi-steady state reduction of molecular motor-based models of directed intermittent search *Bull. Math. Biol.* **72** 1840–66

[22] Bressloff P C and Newby J M 2009 Directed intermittent search for hidden targets *New J. Phys.* **11** 023033

[23] Bressloff P 2006 Stochastic model of protein receptor trafficking prior to synaptogenesis *Phys. Rev.* E **74** 031910

[24] Alami N H, Jung P and Brown A 2009 Myosin Va increases the efficiency of neurofilament transport by decreasing the duration of long-term pauses *J. Neurosci.* **29** 6625–34

[25] Uchida A and Brown A 2004 Arrival, reversal, and departure of neurofilaments at the tips of growing axons *Mol. Biol. Cell* **15** 4215–25

[26] Widder D V 1941 *The Laplace Transform* (Princeton, NJ: Princeton University Press)

[27] Uchida A, Alami N H and Brown A 2009 Tight functional coupling of kinesin-1A and dynein motors in the bidirectional transport of neurofilaments *Mol. Biol. Cell* **20** 4997–5006

[28] Reed M and Blum J J 1994 Mathematical questions in axonal transport *Lectures on Mathematics in the Life Sciences* vol 24 (Providence, RI: American Mathematical Society) pp 1–21

[29] Scott D A, Das U, Tang Y and Roy S 2011 Mechanistic logic underlying the axonal transport of cytosolic proteins *Neuron* **70** 441–54

[30] Roy S, Yang G, Tang Y and Scott D A 2012 A simple photoactivation and image analysis module

for visualizing and analyzing axonal transport with high temporal resolution *Nature Protoc.* **7** 62–68

[31] Weissmann C and Brandt R 2008 Mechanisms of neurodegenerative diseases: insights from live cell imaging *J. Neurosci. Res.* **86** 504–11

[32] Kuznetsov A V, Avramenko A A and Blinov D G 2010 Investigation of the role of diffusivity on spreading, rate, and merging of the bell-shaped waves in slow axonal transport *Int. J. Numer. Methods Biomed. Eng.* **27** 1040–53

[33] Lasek R J, Paggi P and Katz M J 1992 Slow axonal transport mechanisms move neurofilaments relentlessly in mouse optic axons *J. Cell Biol.* **117** 607–16

[34] Monsma P C, Li Y, Fenn J D, Jung P and Brown A 2014 Local regulation of neurofilament transport by myelinating cells *J. Neurosci.* **34** 2979–88